remote sensing

MDPI

Article

Assessing Spatiotemporal Variations of Sentinel-1 InSAR Coherence at Different Time Scales over the Atacama Desert (Chile) between 2015 and 2018

Tobias Ullmann [1,*], Julia Sauerbrey [1], Dirk Hoffmeister [2], Simon Matthias May [2], Roland Baumhauer [1] and Olaf Bubenzer [3]

1 Institute of Geography and Geology, University of Würzburg, Am Hubland, D-97074 Wuerzburg, Germany; julia.sauerbrey@stud-mail.uni-wuerzburg.de (J.S.); baumhauer@uni-wuerzburg.de (R.B.)
2 Institute of Geography, University of Cologne, Zülpicher Straße 45, D-50674 Köln, Germany; dirk.hoffmeister@uni-koeln.de (D.H.); mays@uni-koeln.de (S.M.M.)
3 Institute of Geography and Heidelberg Center for the Environment, University Heidelberg, Im Neuenheimer Feld 348, D-69120 Heidelberg, Germany; olaf.bubenzer@uni-heidelberg.de
* Correspondence: tobias.ullmann@uni-wuerzburg.de; Tel.: +49-(0)-931-31-86865

Received: 4 November 2019; Accepted: 9 December 2019; Published: 10 December 2019

Abstract: This study investigates synthetic aperture radar (SAR) time series of the Sentinel-1 mission acquired over the Atacama Desert, Chile, between March 2015 and December 2018. The contribution analyzes temporal and spatial variations of Sentinel-1 interferometric SAR (InSAR) coherence and exemplarily illustrates factors that are responsible for observed signal differences. The analyses are based on long temporal baselines (365–1090 days) and temporally dense time series constructed with short temporal baselines (12–24 days). Results are compared to multispectral data of Sentinel-2, morphometric features of the digital elevation model (DEM) TanDEM-X WorldDEM™, and to a detailed governmental geographic information system (GIS) dataset of the local hydrography. Sentinel-1 datasets are suited for generating extensive, nearly seamless InSAR coherence mosaics covering the entire Atacama Desert (>450 × 1100 km) at a spatial resolution of 20 × 20 meter per pixel. Temporal baselines over several years lead only to very minor decorrelation, indicating a very high signal stability of C-Band in this region, especially in the hyperarid uplands between the Coastal Cordillera and the Central Depression. Signal decorrelation was associated with certain types of surface cover (e.g., water or aeolian deposits) or with actual surface dynamics (e.g., anthropogenic disturbance (mining) or fluvial activity and overland flow). Strong rainfall events and fluvial activity in the periods 2015 to 2016 and 2017 to 2018 caused spatial patterns with significant signal decorrelation; observed linear coherence anomalies matched the reference channel network and indicated actual episodic and sporadic discharge events. In the period 2015–2016, area-wide loss of coherence appeared as strip-like patterns of more than 80 km length that matched the prevailing wind direction. These anomalies, and others observed in that period and in the period 2017–2018, were interpreted to be caused by overland flow of high magnitude, as their spatial location matched well with documented heavy rainfall events that showed cumulative precipitation amounts of more than 20 mm.

Keywords: Chile; Atacama; Sentinel-1; InSAR; coherence; geomorphology

1. Introduction

The Sentinel-1 mission of the European Space Agency (ESA) delivers temporally dense, high-resolution synthetic aperture radar (SAR) imagery of the Earth´s surface [1]. These C-Band datasets are suited for the characterization of spatiotemporal dynamics (i.e., for the recognition and

identification of land surface changes at a very high level of sensitivity, in a continuous manner, and for large study areas [2]). Sentinel-1 data allow for interferometric SAR (InSAR) applications, including the monitoring and quantification of land surface elevation changes in different environments [2,3]. Advantages of Sentinel-1 data in comparison to preceding civil SAR missions are the large swath width, maintaining phase coherence and a comparably high spatial resolution, and the short temporal revisit period of twelve or six days when Sentinel-1 A and Sentinel-1 B datasets can be combined.

Such InSAR data offer the opportunity to utilize the phase information of two SAR acquisitions in the coherent change detection (CCD) [4–6]. CCD is known to be highly sensitive to changing surface conditions (i.e., dielectric properties and target geometry) and it can be used to identify alterations that are not recognizable in the SAR intensity or in the spectral signal of optical remote sensing imagery [7,8]. Further, CCD is sensitive to changes on the subpixel scale, since it utilizes phase and intensity information of the electromagnetic wave coherently [5,9]. However, the applicability of CCD is limited by the temporal delay between the acquisitions, where longer temporal baselines usually cause a loss of coherence. Further, CCD requires a suited acquisition geometry (i.e., usually repeated observations from a similar orbit position).

The high potential of InSAR datasets in change detection has been demonstrated in previous studies, exemplarily on risk and damage assessment after natural or anthropogenic disasters [6,10–12]. Further, previous studies also highlight the application of CCD in physiogeographical research, and particularly in geomorphological contexts. In this field of geoscience, CCD is especially promising for applications in arid and semiarid environments, as here the rather short stature of the vegetation and the usually low vegetation fraction coverage (if any) advance high InSAR coherence and allow for area-wide investigations. The applicability of CCD in the C-Band and for arid environments has been shown for European Remote Sensing (ERS) satellite datasets [13–16], as well as more recently for Sentinel-1 datasets [8,17–19]. In regard to these studies, it can be summarized that CCD is a highly sensitive method for characterizing different physical surface properties and identifying (changing) surface conditions. Exemplarily, increased soil moisture, sediment transport, and anthropogenic activity may be detected, as such events manifest by either a temporal or a permanent loss of InSAR coherence due to changes of the target's dielectrical or geometrical properties. The application of InSAR coherence in change detection faces difficulties in rugged and mountainous terrain and over surfaces that generally appear as noncoherent in the imagery. Further, available temporal and spatial baselines, as wells as SAR systems' capacities (coverage, geometrical resolution, and revisit time), can limit the applicability of CCD.

Regarding the new capacities of the Sentinel-1 mission, we assess spatiotemporal variations of Sentinel-1 InSAR coherence on different time scales acquired over the Atacama Desert (Chile) between 2015 and 2018. Our investigations aim at (i) distinguishing different desert surface areas, which are associated with diverging morphodynamic characteristics; and (ii) determining factors that are responsible for these differences and for the observed spatial or temporal changes. Therefore, the Sentinel-1 time series features are compared to morphometric and hydrographic features deduced from TanDEM-X WorldDEM™, temporal-matching multispectral features of Sentinel-2, and a highly detailed governmental geographic information system (GIS) dataset on the local hydrography. Ultimately, our approach may contribute to the establishment of new techniques for arid landscape characterization, aiming at better understanding landscape dynamics and geomorphological processes in arid to hyperarid environments.

2. Materials and Methods

2.1. Study Area

The hyperarid core of the Atacama Desert stretches between 22°–25° S (Figure 1) and experiences <10 mm/year rainfall on average [20]. Hyperaridity is caused by a combination of subtropical subsidence [21], coastal upwelling of the Peru–Chile Current [22], and rain-shadow effects of the

Andes [20], and is thought to have been established around the mid-Miocene or earlier [23,24]. Precipitation generally increases north-, east-, and southwards due to convective rainfall from tropical easterlies in the Andes and the increased influence of southern westerlies in austral winter [25]. Marine fog frequently occurs until ~1200 m above sea level [26,27] along the western slopes of the Coastal Cordillera but may extend farther inland depending on local topography [28]. This constellation results in the typical climatic and morphodynamic zonation of the Atacama (Figure 1d), with the driest parts of the Atacama being located between the coastal ranges and the pre-Andean cordilleras, including the Central Depression, which are framed by extensive and episodically active alluvial fan systems in the east and the fog-affected western slopes of the Coastal Cordillera in the west.

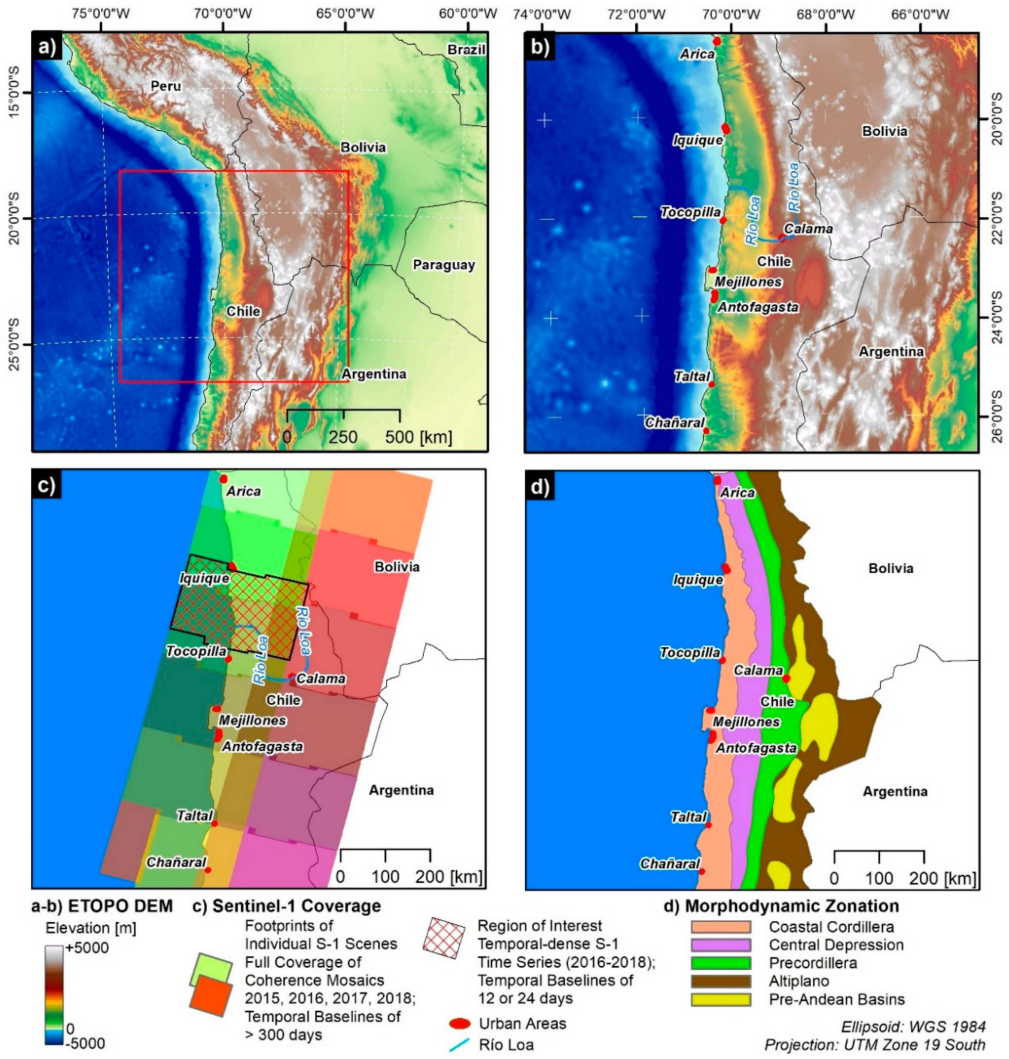

Figure 1. Study area and data coverage: (**a**) regional overview; (**b**) topographic setting and major cities; (**c**) footprints of Sentinel-1 imagery (2015, 2016, 2017, and 2018) and location of region of interest (ROI); (**d**) morphodynamic zonation. The red rectangle in (a) shows the extent of panels (b–d). Note: ETOPO DEM = Earth Topography Digital Elevation Model (www.ngdc.noaa.gov/mgg/global/).

As generally proposed for hyperarid deserts, geomorphic processes in the Atacama are suggested to be of remarkable slowness, as evidenced by the age of surfaces and landforms [23,29,30]. Numerous landforms in the Atacama may thus represent fossil evidence of past geomorphic activity [31], especially in the central desert, which is typically disconnected from both fog-related atmospheric moisture and Andean discharge. However, severe precipitation events followed by overland flow or flash flood activity may even reach hyperarid parts of the Atacama, as documented by the March and August

2015 and June 2017 rainfall events [19,32,33]. The 2015 events are in relation to the El Niño–Southern Oscillation (ENSO) (Figure 2b).

Smooth slope morphologies typically result from thick atmospherically derived salt and dust deposits masking hillslopes in the central desert, where soils contain large amounts of salts, such as nitrate, iodate, and the common sulphates gypsum and anhydrite [34–36]. This atmospheric deposition is thought to be supported by biological soil crusts [37] and may lead to salt-dominated soils and a remarkable volumetric expansion under long-term hyperaridity. Salt-driven shrink–swell, slumping, or solifluction-type processes are, thus, thought to be responsible for various landforms in the central desert [38]. Finally, seismicity-driven processes are actively shaping surfaces in the driest parts of the Atacama, as has been shown recently [30,39,40].

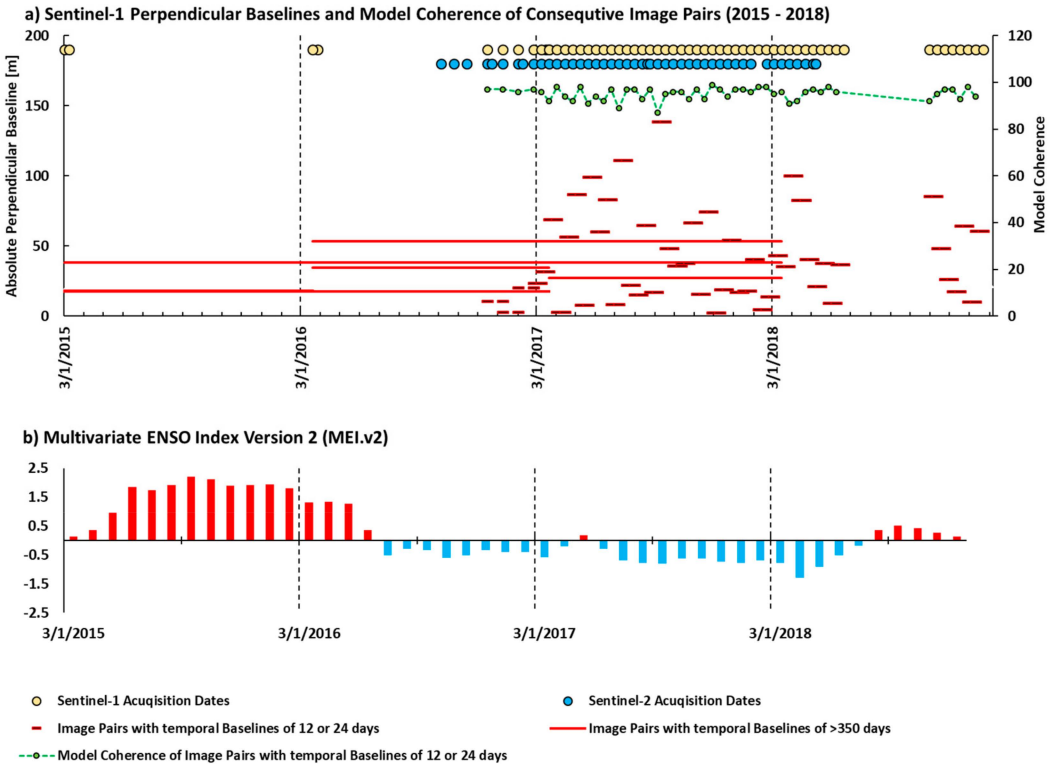

Figure 2. Overview of synthetic aperture radar (SAR) acquisition geometry and Multivariate El Niño–Southern Oscillation (ENSO) Index values: (**a**) Sentinel-1 and Sentinel-2 acquisition dates, perpendicular baselines, and model coherences of all investigated Sentinel-1 image pairs recorded in interferometric SAR (InSAR) repeat-pass configuration using the same relative orbits; (**b**) Multivariate ENSO Index Version 2 (MEI.v2) (esrl.noaa.gov/psd/enso/mei).

2.2. Sentinel-1

Two sets of Sentinel-1 VV/VH-polarized interferometric wide-swath (IW) data were investigated for this study. The first set was compiled to cover the full area shown in Figure 1c (approximately 450 × 1100 km), using twelve single scenes acquired in March of a certain year (2015–2018) (Figure 2a), and along one relative orbit running in the north–south direction. Long temporal baselines of 385 days (2015–2016), 367 days (2016–2017), and 361 days (2017–2018) were derived. The longest investigated temporal baseline was 1093 days for the image pair 2015–2018. The second set contained a stack of 52 images acquired with short temporal baselines of 12 or 24 days between December 2016 and December 2018 over a specific region of interest (ROI, Figure 1 c; coverage of approximately 120 × 180 km) in the center of the Atacama Desert, ranging from the coast to the Central Depression. Regular observations at 12 or 24 day intervals are available starting from December 2016. Figure 2a indicates the acquisition dates and the perpendicular baselines of all investigated Sentinel-1 image pairs. In addition, the model

coherence is shown for the second set. Model coherence is an estimator for the expected decorrelation and its calculation is solely based on the perpendicular baseline, the temporal baseline, and the mean Doppler centroid frequency difference. The values of the model coherence were linearly scaled to a range from 0 to 100; higher values indicate a higher suitability for InSAR analysis.

The data were downloaded as single-look complex (SLC) products from the Sentinel hub and underwent the processing illustrated in Figure 3. The processing was adapted from [8,18], but the derivation of polarimetric features was included. The following SAR features were processed in SNAP 6 (step.esa.int/main/toolboxes/snap/) and IDL/ENVI 5.3 (www.harrisgeospatial.com). First, the terrain-corrected gamma nought VV and VH intensities were processed (Figure 3a). The intensity information of the same relative orbits was compared and information was scaled to decibels. Second, polarimetric features of dual-polarization entropy/alpha decomposition [41,42] were processed using the covariance matrix (C2) and the VV/VH-polarized Kennaugh matrix [43] (Figure 3a). Third, interferometric (InSAR) coherences of the VV and VH channels were deduced after coregistration (Figure 3b), but analysis concentrated on the copolarized channel (VV). The time series was set up using sequential masters [44] and the master image was the one acquired first. The flat-earth phase and topographic phase were removed using TanDEM-X WorldDEM™ (see below).

The InSAR coherence γ is a measure for the correlation of the complex signals of two SAR acquisitions. It utilizes the phase information of both signals, making the feature highly sensitive to changing target properties [9,13] (Equation (1)).

$$\gamma = \frac{E\left\{s_1^* \cdot s_2\right\}}{\sqrt{E\left\{|s_1|^2\right\} \cdot E\left\{|s_s|^2\right\}}} \quad (1)$$

where $E\{\}$ is the expectation value, s_1 and s_2 are the backscattered signals, and s^* describes the complex conjugate of s. The correlation coefficient γ can be estimated directly from the two datasets [9,18]. The coherence ranges from zero to one, where zero indicates total signal decorrelation and one indicates full signal correlation. InSAR coherence is affected by several types of decorrelation (Equation (2)) [9]:

$$\gamma = \gamma_{temp} \cdot \gamma_{SNR} \cdot \gamma_{geo} \cdot \gamma_{vol} \quad (2)$$

where γ_{temp} denotes temporal correlation and addresses geometrical and dielectrical changes between the acquisitions; it is usually the dominant factor altering the coherence in repeat pass CCD. Here, γ_{SNR} accounts for thermal, instrument, and processor noise, while γ_{geo} quantifies the influences caused by the acquisition geometry; γ_{vol} accounts for the effect of volume or random scattering. The relevance of the listed factors on InSAR coherence is discussed in detail in [7,9,10,45].

The analysis of the first set concentrated on the COH VV, while for the second set, four SAR features were considered: K0 (total intensity of VV and VH), entropy (degree of scattering randomness ranging from 0 (low) to 1 (high)), VV InSAR coherence (COH VV), and VH InSAR coherence (COH VH). All of the features were processed to a spatial resolution of 20 × 20 m per pixel (World Geodetic System (WGS) 1984/ Universal Transverse Mercator (UTM) Zone 19 South, European Petroleum Survey Group Geodesy (EPSG): 32719). Additionally, the temporal features minimum, maximum, mean, median, and standard deviation were calculated in the temporal dimension of the stack (Figure 3c) [8]. Hereafter, the mean images of a certain feature are denoted with "μ"; images of the standard deviation of a certain feature are denoted with "σ".

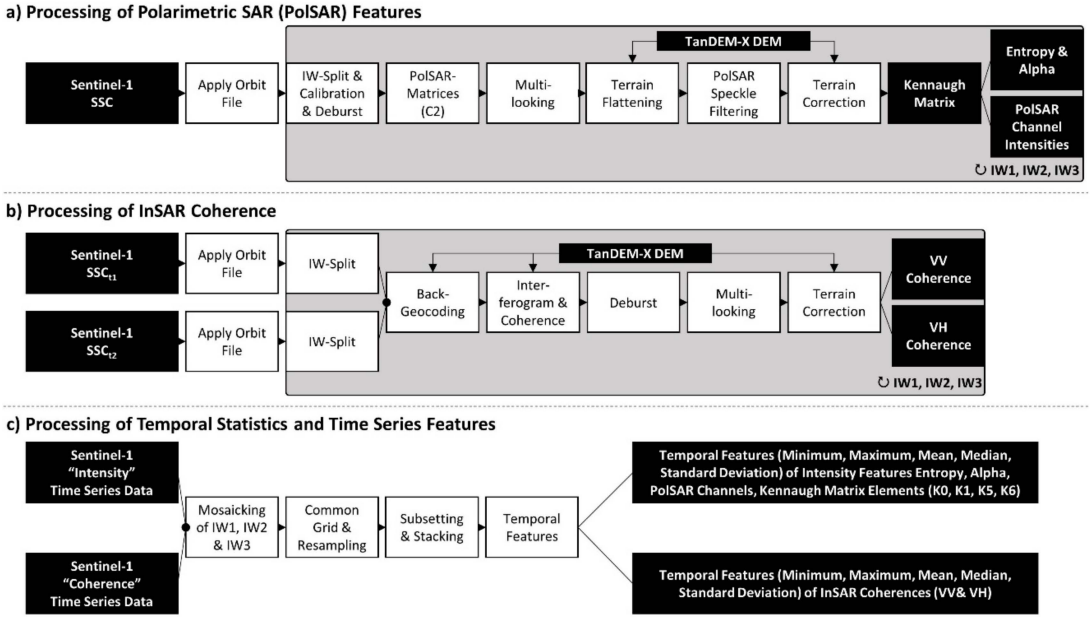

Figure 3. Processing of Sentinel-1 data: (**a**) processing of polarimetric features using the covariance and the Kennaugh matrix; (**b**) processing of InSAR coherences; (**c**) processing of temporal statistics and time series features. Note: SSC = Single Look Slant Range Complex-; IW = interferometric wide-swath.

2.3. Reference and Auxiliary Datasets

Sentinel-1 features were compared to morphometric and hydrographic features deduced from the TanDEM-X WorldDEM™ and to (temporally matched) surface reflectance values and tasseled cap transformation (TC) features of Sentinel-2 [46,47]. Additionally, a freely available and highly detailed governmental GIS compilation of the hydrographic channel network of Chile was used as a reference (http://bcn.cl/siit/mapas_vectoriales). The results were further compared to documented rainfall events of high magnitude that also reached parts of the hyperarid core of the Atacama Desert. These events happed in the periods 2015–2016 (March and August 2015) and 2017–2018 (June 2017), and are described in detail by [19,33,48].

Six individual tiles of Sentinel-2 covered the study area (ROI) and all available scenes with cloud cover of less than 20% were considered for the analysis, so that the best possible temporal match with the Sentinel-1 acquisitions was reached (Figure 2). The level 1C datasets were geometrically corrected and the per-pixel radiometric measurements were given in top of atmosphere (TOA) reflectance [49]. The software "Sen2Cor" was used [50] to generate terrain and atmospherically corrected bottom of atmosphere (BOA) reflectance values. For all tiles, BOA reflectance was deduced and datasets were clipped, mosaicked, and gridded (WGS 1984/UTM Zone 19 South, EPSG: 32719). In addition, the features of the TC [46] were processed. TC generates the main transformations features "brightness", "greenness", and "wetness" [47]. As suggest by the index database (IDB, indexdatabase.de), TC was computed using the same coefficients as for Landsat 8, choosing the bands of matching wavelengths.

A TanDEM-X WorldDEM™ dataset, in figures denoted as "TanDEM-X DEM", was made available for this study by the German Aerospace Center (DLR) via a science grant (see Acknowledgments) [51]. This DEM was shown to be of high accuracy and quality in previous studies [52,53], and also in the context of geomorphological applications [54–56]. The DEM covered the ROI (Figure 1) and had a pixel spacing of 12 m (WGS 84/UTM Zone 19S, EPSG: 32719). The DEM underwent hydrographic modeling in SAGA GIS Version 5 (http://saga-gis.org), and the multiflow direction (MFD) flow accumulation was processed [57,58]. The elevation data and the MFD were further used to estimate the topographic wetness index (TWI) [57].

3. Results

3.1. Sentinel-1—Long Temporal Baselines

The VV coherence mosaics of the Atacama Desert for periods 2015–2016 (Figure 4a), 2016–2017 (Figure 4b), 2017–2018 (Figure 4c), and 2015-2018 (Figure 4d) were constructed with temporal baselines of 385, 367, 361, and 1093 days, and corresponding perpendicular baselines of 18, 34, 27, and 38 m. The mosaics are nearly seamless and borders between neighboring scenes of different relative orbits are hardly visible. For all periods, characteristic domains appear in the imagery that could be linked with the morphometric zonation of the Atacama Desert (Figure 1d): the uplands of the Coastal Cordillera, the central desert, and the alluvial fans west of the Precordilleras show very high InSAR coherences in all periods, with values greater than 0.85 for most regions (>70% of the area). Regions in the Andes and the Altiplano that are characterized by a mountainous setting are characterized by lower and more variable InSAR coherence values. Here, the influence of radar effects (i.e., shadowing, foreshortening, and layover) on the InSAR coherences is clearly visible and leads to spatial and temporal inconsistencies of the signal.

The histograms of the coherence images for 2015–2016, 2015–2017, and 2015–2018 show a continuous decrease of coherence values with increasing temporal baseline (histograms in Figure 4), which is attributed to the temporal decorrelation, as perpendicular baselines of all image pairs are similar. Notably, 75% of all InSAR coherence values are above a value of 0.7 for the period 2015–2018, even though the temporal baseline is 1093 days. The median values are 0.85 (2015/2016), 0.83 (2015–2017), and 0.81 (2015–2018), meaning all mosaics of all temporal baselines show median values above 0.8 and lower quartile values above 0.55.

Remarkable anomalies in the InSAR coherence mosaics (Figures 4 and 5) are found in relation to the drainage network for periods 2015–2016 (between Antofagasta, Tocopilla, and Calama) and 2017–2018 (more locally in the east and southeast of Antofagasta). The InSAR coherence anomalies perfectly match the channel courses of the reference datasets (Figure 5) between Taltal and Arica for the period 2015–2016, meaning the differences of the coherence values over the reference drainage channels are in the order from −0.4 to −0.8 (displayed in profile AB at distance 4700 m in Figure 5k).

Regions where such linear anomalies were found frequently also show patterns of area-wide loss of InSAR coherence. Such patterns appear as NW–SE-oriented stripes of lower coherence, with lengths of more than 80 km in the coherence image mosaic for 2015–2016. This area-wide and extensive loss of InSAR coherence is exemplarily displayed in the subsets of Figure 5i,j. The drop of coherence in profile EF between 6000 m and 8000 m (Figure 5m) is approximately −0.3.

These observations also appear clearly in the difference images of the 2015–2016, 2016–2017, and 2017–2018 coherences (Figure 6), and spatial anomalies with a coherence loss of <−0.3 appear as strip patterns over the Central Depression and the Precordillera (indicated with blue color in Figure 6a). The extensive and area-wide loss of coherence is further also coupled with the associated channel network of matching watersheds (see Figure 5 in addition). Similar, Figure 6b shows anomalies in the coherence mosaics 2016–2017 and 2017–2018 in the east and southeast of Antofagasta (indicated with yellow and red colors in Figure 6b). Finally, loss of coherence between 2015 and 2016 is also observed at the westward-facing slopes of the Coastal Cordillera north of Tocopilla and south of Antofagasta.

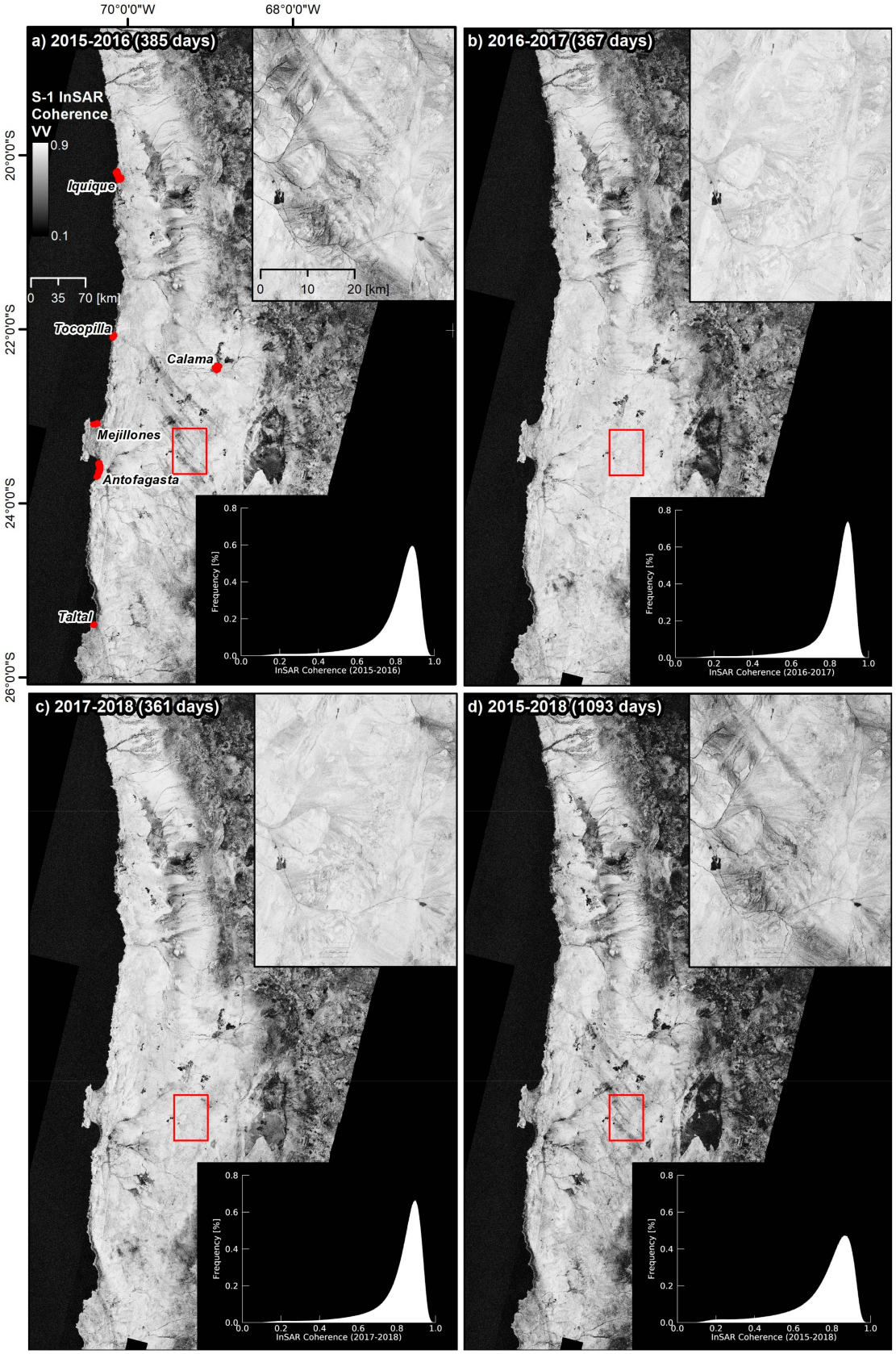

Figure 4. Overview of the processed Sentinel-1 InSAR VV coherence mosaics: (**a**) March 2015 and March 2016 (385 days); (**b**) March 2016 and March 2017 (367 days); (**c**) March 2017 and March 2018 (361 days); (**d**) March 2015 and March 2018 (1093 days).

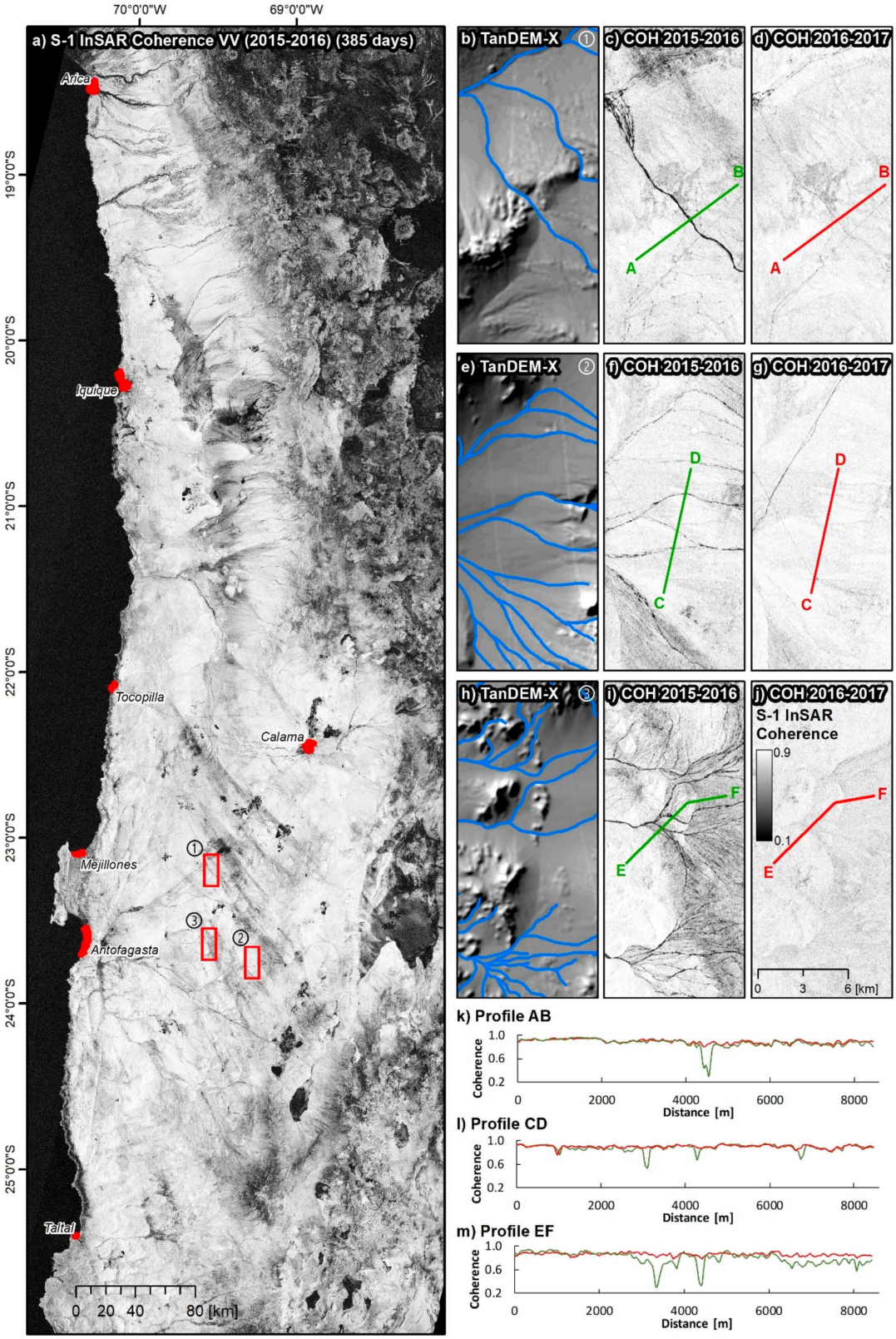

Figure 5. Example of detection of fluvial activity: (**a**) Sentinel-1 InSAR VV coherence mosaic of March 2015 to March 2016 (385 days); (**b**,**e**,**h**) TanDEM-X WorldDEM™ hill shades and channel network; (**c**,**f**,**i**) InSAR VV coherences (2015–2016); (**d**,**g**,**j**) InSAR VV coherences (2016–2017); (**k**,**l**,**m**) profile plots of coherence (COH) for 2015–2016 (light green) and 2016–2017 (dark red).

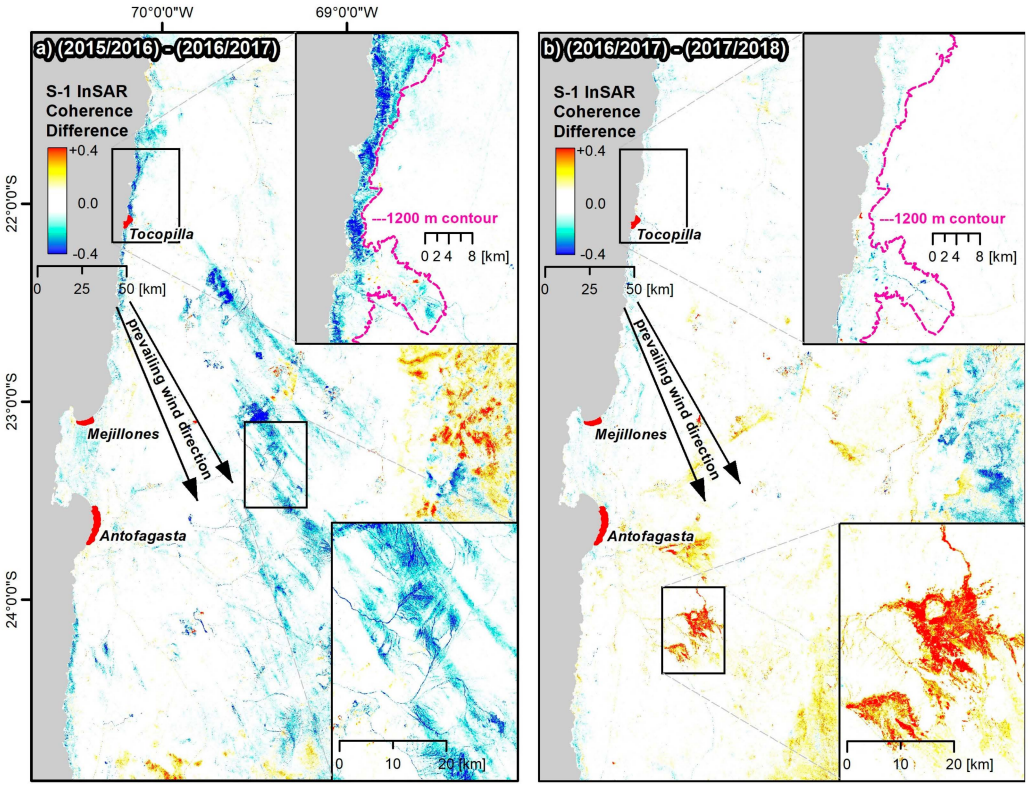

Figure 6. InSAR coherence difference maps: (**a**) VV coherence difference for (2015/2016)–(2016/2017) and (**b**) (2016/2017)–(2017/2018). Coherences anomalies in the lower enlargement (**a**) are related to heavy precipitation events that happened in March and August 2015, while anomalies in enlargement (**b**) are related to rainfall events >20 mm that occurred 6–7 June 2017 [33].

3.2. *Sentinel-1—Short Temporal Baselines*

3.2.1. Relation of SAR Time Series Features to Geomorphic Domains

The time series features of COH VV and K0 for the second set (constructed with short temporal baselines of 12/24 days) are exemplarily shown in Figure 7 in comparison to a true color RGB of Sentinel-2 and the TanDEM-X WorldDEM™. The visual inspection allowed characterization of several domains by μ K0 intensity values—the steep slopes of the coastal area, the Salar Grande, the Salar de Bella Vista, the Salar de Llamara, as well as the bedrock outcrops of the Coastal Cordillera and the slopes of the Precordillera show high μ K0 values above −10 dB. In contrast, low μ K0 values (<−15 dB) are observed for the alluvial plains of the Central Depression (see Figure 7c and P3 in Figure 7g). The lowest K0 values are found for locally active sand dune systems south of the Pica Sand Dunes (see below) at the transition between the Central Depression and the Precordillera. Here, μ K0 values were in the order of <−20 dB. The intensity is most variable over time for the salt lakes (σ K0 of approximately 2 dB; see P1 in Figure 7g) and the steep slopes of the Precordillera (σ K0 > 2 dB). However, for most parts of the ROI (>77.5% of the area), the temporal signal variations of K0 are <1 dB on average (e.g., see P4 in Figure 7g), indicating similar backscattering over time. The most significant changes (>3 dB) can be attributed to mining activity, best visible for the large mining area between the Salar Grande and the Salar de Bella Vista. The μ COH VV (Figure 7e,f) showed a clear division of the ROI into characteristic domains. The alluvial plains of the Central Depression are characterized by comparably low values of approximately 0.3 to 0.8 (see P3 in Figure 7h), whereas most other regions show very high values of above 0.8 (>69.2% of the area) beside areas of active mining that are frequently indicated by lower values, and the mentioned dune systems that are characterized by μ COH VV of <0.2. Further, the mining areas show the highest σ COH VV values of >0.15 (Figure 7h).

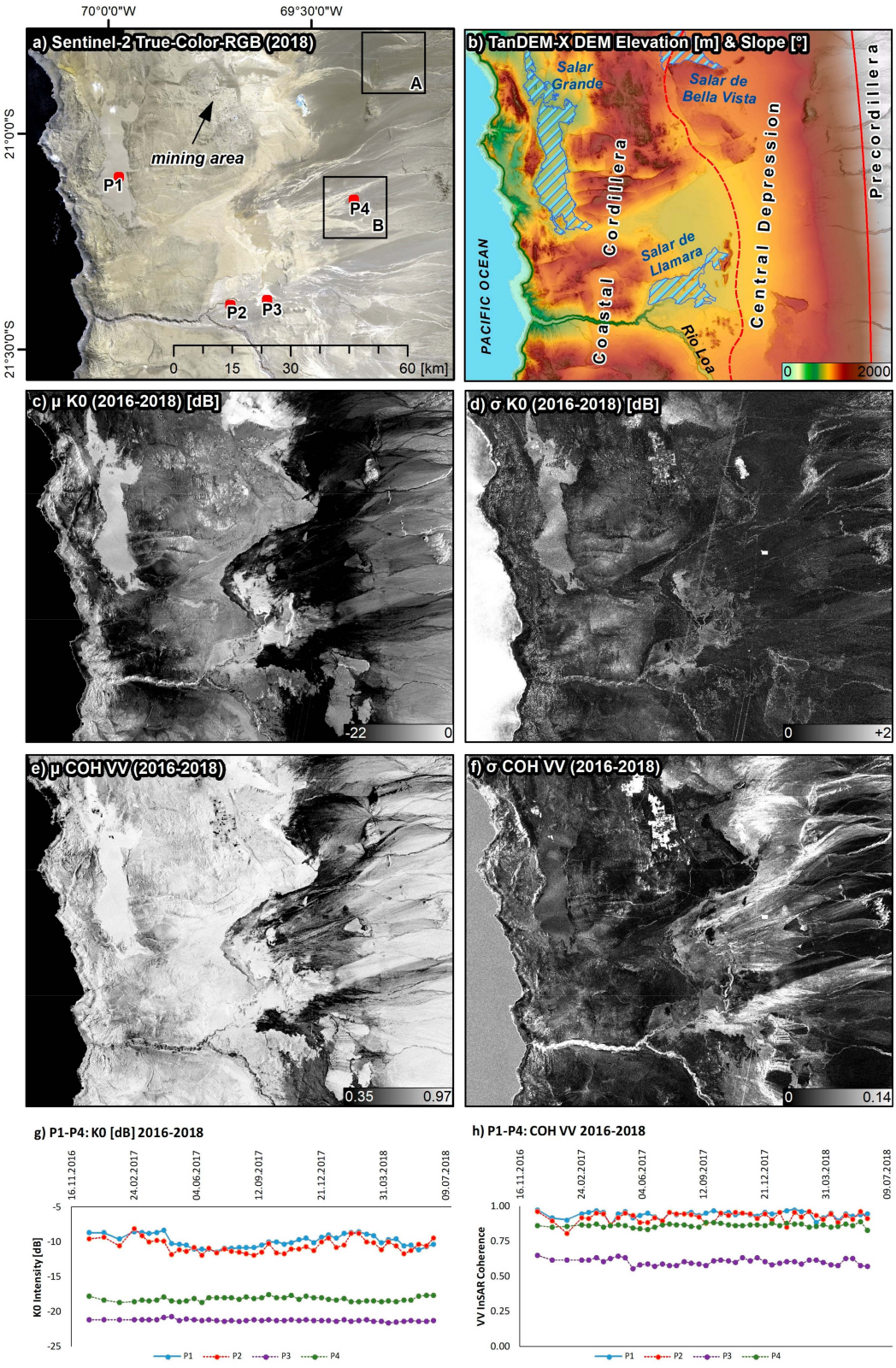

Figure 7. Features utilizing the temporally dense stack of Sentinel-1 acquisitions: (**a**) RGB true color composite of a Sentinel-2 acquisitions; (**b**) TanDEM-X WorldDEM™; (**c**) μ of K0 intensity; (**d**) σ of K0 intensity; (**e**) μ of VV coherence; (**f**) σ of VV coherence; temporal signatures of P1 to P4 of (**g**) K0 intensity (dB); (**h**) VV coherence. Signatures show the average of a 9 × 9 pixel window centered on the point of interest.

Other regions that are indicated by comparably high temporal variations (σ COH VV in the order from 0.10 to 0.15) are found over the alluvial plains of the Central Depression (see P3 in Figure 7g,h) and along the deeply incised valley of the Rio Loa. However, most locations inside the ROI display σ COH VV <0.1 and σ COH VH <0.05 (>80.5% of the area), indicating very stable target properties when 12 or 24 day temporal baselines are investigated.

In this context, Figure 8 presents an example of two sites inside the ROI with known aeolian sandy deposits that appear as noncoherent targets in the imagery [59]. They are situated on, or close to, local bedrock outcrops or alluvial fans at the transition between the Central Depression and the Precordilleras, approximately 40 km south of the Pica Sand Dunes. Their genesis is likely linked to the adjunct alluvial plain and local main wind directions from the west or southwest [59]. The dune belt stretches northeast–southwest and is visually recognizable in the optical imagery (Figure 8d,h). In the SAR features, the deposits are characterized by very low μ COH VV (<0.3) and by very high polarimetric μ entropy values close to 1.0. Notably, σ COH VV is high (>0.1) at the outer fringes of the single dunes (Figure 8b,f). Compared to other sites, the COH VV and entropy generate a distinct SAR signature, and these sandy aeolian sediments are clearly recognizable in the imagery.

Similar to the results obtained from the long temporal baselines, linear anomalies in correspondence to the reference channel network were found in the InSAR coherence imagery processed at short temporal baselines. Location "B" in Figure 7a shows a region where such linear anomalies are detected between December 2016 and December 2018. The site is located inside the ROI at the transition from the Precordillera to the alluvial plain. Here, the local bedrock is cut by several incised parallel channels that merge at the foot of the slope into the alluvial plain.

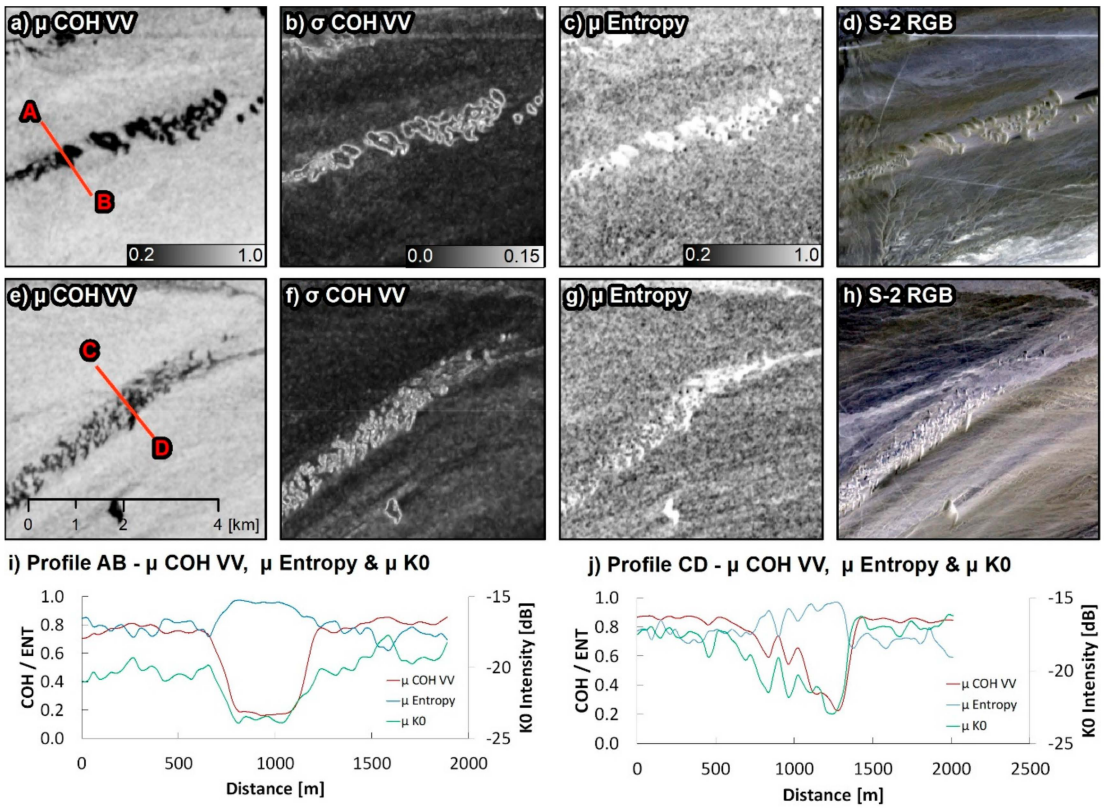

Figure 8. Example of aeolian sediment coverage (south of the Pica Sand Dunes) utilizing the temporally dense stack of Sentinel-1 acquisitions (location "A" in Figure 7a): (**a**,**e**) μ of VV coherence; (**b**,**f**) σ of VV coherence; (**c**,**g**) μ entropy; (**d**,**h**); RGB true color composites of selected Sentinel-2 acquisitions; (**i**,**j**) profile plots of μ of VV coherence, μ entropy, and μ K0 intensity.

The μ COH VV (Figure 7e) indicates that the mean VV coherence of this region is on average moderately high (about 0.6), and similarly standard deviation is moderately high (approximately 0.1). The analysis of COH VV imagery for December 2016 to March 2017 (Figure 9a–d) showed a distinct drop of VV coherence of approximately −0.5 (Figure 9i) between 8 January 2017, and 20 January 2017, over some of the channels. The identified locations match the course of the reference channels of the drainage network (not shown). The drop is only observed in a single image pair and coherence values recover to the pre-event level for image pairs acquired after 20 January 2017.

Notably, a smaller second anomaly is found between 25 February 2017, and 9 March 2017. The data indicate a second drop in the coherence (at distance 2.9 km) by −0.4 (Figure 9i) compared to the pre-event level. The main event (between 8 and 20 January 2017) is also displayed in the optical TC datasets of Sentinel-2. The RGB composites of the TC features brightness, greenness, and wetness are shown for the acquisition dates 13 November 2016, 1 February 2017, 21 February 2017, and 13 March 2017 in Figure 9e–h (available cloud-free acquisitions). All features of the TC show a change in values after the main discharge event. The variation is clearest in the TC greenness and brightness and changes are about +0.5 (brightness) (Figure 9j) and +0.16 (greenness) (Figure 9k). In contrast to the COH VV, the values of the TC did not recover to the pre-event level, but stayed at the same level once the event happened.

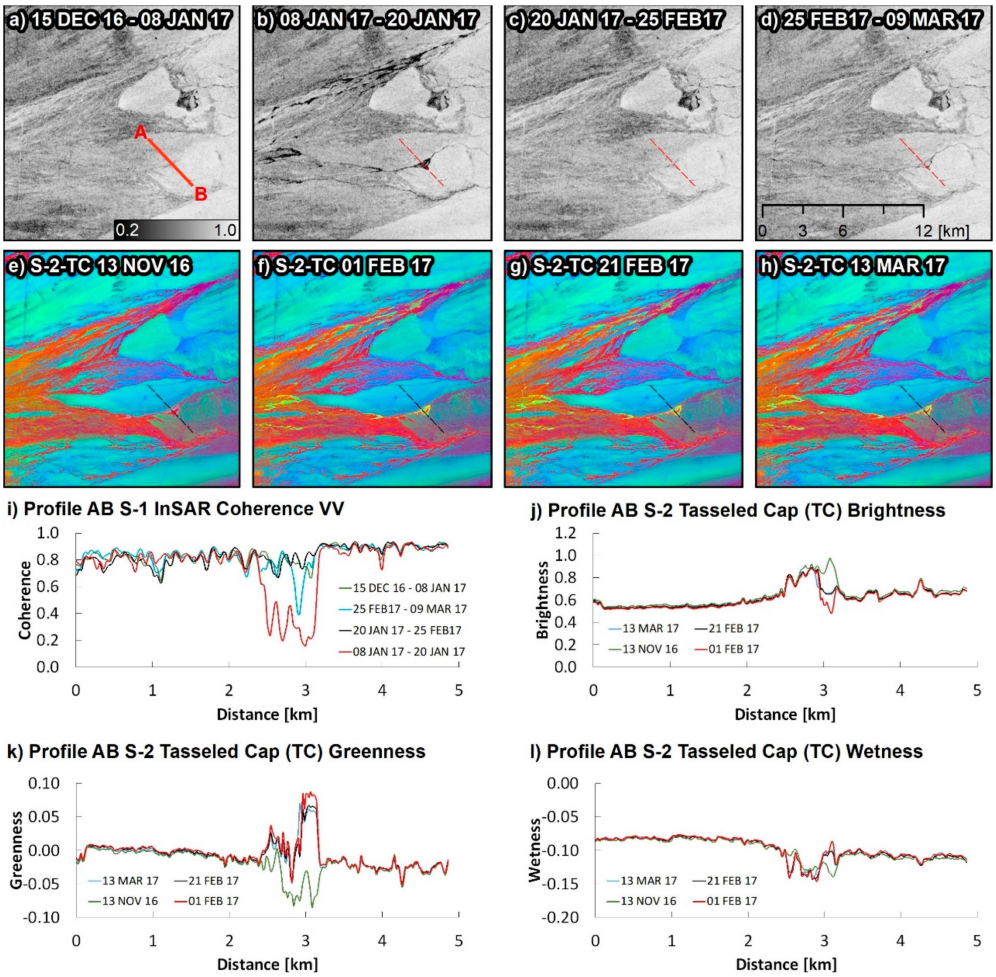

Figure 9. Example of detection of fluvial activity utilizing the temporally dense stack of Sentinel-1 acquisitions (location "B" in Figure 7a): (**a**–**d**) selected VV coherences (12 day temporal baselines); (**e**–**h**) RGB false color composites of temporally matching Sentinel-2 acquisitions using tasseled cap features for brightness (R), greenness (G), and wetness (B); (**i**–**l**) profile plots of the investigated features for dates before and after the fluvial event.

3.2.2. Influence of the Acquisition Geometry

Further analyses focused on the overall statistics of the second set of VV InSAR coherences. The image statistics of COH VV are compared to the corresponding perpendicular baselines and the model coherences in order to indicate the influence of the acquisition geometry on the actual coherence values. The median COH VV values of the ROI (excluding water surface) range between 0.85 and 0.91 for all 51 scenes (2016–2018). The maximum values are close to 1.0, whereas the values of the lower quartile (LQ25%) range between 0.75 and 0.82. Similar, the model coherence varies between values of 87 and 99, while all perpendicular baselines range between 5 and 140 m. COH VV LQ25%, median, and values of the upper quartile (UQ75%) are highly correlated with squared Pearson's correlation coefficients (R^2) of 0.94 (median and LQ25%), 0.97 (median and UQ75%), and 0.85 (LQ25% and UP75%). The R^2 value for the COH VV median and the perpendicular baseline is 0.40 and for the COH VV median and the model coherence is 0.43.

3.2.3. Relation of InSAR Coherence to SAR/DEM Features

The temporal means and the standard deviations of the Sentinel-1 features K0 (Figure 7c,d), entropy, COH VV (Figure 7e,f), and COH VH are analyzed in simple linear regression modeling (Table 1) in order to indicate dependencies of InSAR coherence to other SAR/DEM features. The analysis is carried out for the ROI (Figure 1c), excluding water. Parameters μ K0 and μ COH VV are positively correlated with a R value of +0.65. Similarly, while μ K0 and μ COH VH are positively correlated with a R value of +0.84. InSAR coherences of both channels (VV/VH) are positively correlated with a R value of +0.80. The standard deviations of VV and VH coherence (σ COH VV and σ COH VH) are not correlated with any other feature (|R| < 0.5), but with themselves with a R value of +0.65. The correlation between SAR and DEM features is generally low and does not exceed |R| values of 0.49. Notably, the μ entropy is only weakly negatively correlated with the μ VV COH (R of −0.47), μ VH COH (R of −0.21), and μ K0 (R of −0.37).

Table 1. Correlation matrix of investigated features shown as linear Pearson's correlation coefficient (R). Statistics are drawn for the region of interest (ROI) and for land surface, excluding water. Note: TWI = topographic wetness index.

	DEM	Slope	TWI	μ K0	σ K0	μ Entropy	σ Entropy	μ COH VV	σ COH VV	μ COH VH	σ COH VH
DEM	1.00	0.53	−0.58	0.41	0.28	−0.19	0.08	0.14	0.22	0.23	0.25
Slope	0.53	1.00	−0.69	0.49	0.42	−0.14	0.09	0.05	0.42	0.28	0.35
TWI	−0.58	−0.69	1.00	−0.36	−0.25	0.21	0.03	−0.22	−0.10	−0.33	−0.16
μ K0	0.41	0.49	−0.36	1.00	0.47	−0.37	0.09	0.65	0.07	0.84	0.13
σ K0	0.28	0.42	−0.25	0.47	1.00	−0.21	0.40	0.05	0.39	0.25	0.38
μ Entropy	−0.19	−0.14	0.21	−0.37	−0.21	1.00	−0.33	−0.47	0.08	−0.21	−0.33
σ Entropy	0.08	0.09	0.03	0.09	0.40	−0.33	1.00	−0.01	0.25	−0.09	0.41
μ COH VV	0.14	0.05	−0.22	0.65	0.05	−0.47	−0.01	1.00	−0.55	0.80	−0.17
σ COH VV	0.22	0.42	−0.10	0.07	0.39	0.08	0.25	−0.55	1.00	−0.23	0.65
μ COH VH	0.23	0.28	−0.33	0.84	0.25	−0.21	−0.09	0.80	−0.23	1.00	−0.18
σ COH VH	0.25	0.35	−0.16	0.13	0.38	−0.33	0.41	−0.17	0.65	−0.18	1.00

4. Discussion

The Sentinel-1 orbital tube generated small and InSAR-suited baselines that were in the range of several meters up to 140 m for all investigated periods. Notably, perpendicular baselines for temporal baselines >300 days and >1000 days were in the order of 35 m, which underlines the very high precision of the system and the fulfillment of the mission requirements [2]. As expected, larger perpendicular baselines led to lower coherence values; vice versa, shorter perpendicular baselines led to higher coherence values, shifting the frequency distribution towards higher values. In this high coherence environment, the varying baselines had only a very small impact on the actual coherence values and did not restrict the image interpretation. Therefore, the Sentinel-1 acquisitions offered a very good and stable setting for CCD analyses.

Given the maturity of the Atacama landscape and the remarkable slowness of processes of the Earth's surface under the prevailing and long-term hyperaridity, numerous landforms can be regarded as fossil evidence of past geomorphic activity [23,29,31]. This results in high InSAR coherence in the C-Band for large parts of the Atacama; however, recent episodic or periodic geomorphic processes–such as overland flow or channel activity during rare but strong precipitation events probably related to ENSO, haloturbation, slumping, or seismic shaking—seem to actively contribute to the landscape characteristics, as shown by [30,32,38–40,60]. Therefore, the Sentinel-1 mission is exceptional in offering Atacama-wide and continuous long-term observations, while gathering information that is highly sensitive to changing surface conditions. For the first time, this study presents a comprehensive analysis of CCD in the C-Band for the entire Atacama Desert at different time scales.

4.1. Long Temporal Baseline Mosaics

The analyses carried out by investigating long temporal baselines (360 to 1090 days) revealed remarkable anomalies in the InSAR coherence mosaics (Figures 4 and 5) in relation to the drainage network for the periods 2015–2016 (between Antofagasta, Tocopilla, and Calama) and 2017–2018 (more locally in the east and southeast of Antofagasta), and in relation to anthropogenic disturbance (especially mining).

Even though no in situ reference for the activity of the channels existed, it is very likely that the observed linear coherence anomalies are linked to the discharge, as the shapes of the anomalies matched the reference drainage network and the hydrographic and topographic setting deduced from the DEM. The differences in coherence between an active channel and its immediate surroundings were distinct and ranged up to 0.6. However, the detection of such events essentially requires a high signal correlation over time (i.e., the regions must be indicated by a high coherence in order to enable a detection). This makes the technique exclusively suited for arid environments; considering the high sensitivity of C-Band SAR data to vegetation, the applicability of the approach will be smaller for regions with higher vegetation fraction coverage.

The coherence mosaics were, therefore, used to trace and delineate area-wide channel activity, and it is possible to compare the spatiotemporal patterns of activity between different periods with high spatial details. For example, fluvial activity was observed between Antofagasta, Tocopilla, and Calama in the period March 2015 to March 2016. In the period March 2017 to March 2018, channel activity was observed more locally in the east and southeast of Antofagasta. In contrast, no events were detected in the period March 2016 to March 2017. This is in accordance with the reported rainfall and precipitation events [33,48] that reached the inner Atacama Desert (e.g., the region east and southeast of Antofagasta experienced a strong precipitation event on 6–7 June 2017 [33].

Interestingly, regions where discharge occurred frequently also show patterns of area-wide loss of coherence in the immediate surroundings and the matching watersheds. This area-wide loss of coherence (approximately −0.3 on average) appeared as northwest–southeast-oriented strips of low coherence in the period 2015–2016. The anomalies were interpreted to be related to strong precipitation events that caused overland flow and fluvial discharge, or that led to a significant increase of the soil moisture causing a meaningful change of dielectric properties. The orientation of these patterns matched the prevailing wind direction and they must be associated with strong rainfall and floods that are reported for March and August 2015 [19,32,48] and June 2017 [33] (i.e., the locations of significant loss of coherence matched with documented heavy precipitation events with cumulative amounts of >20 mm [33]). Further, a previous study [48] analyzed the climatic situation that caused the extensive precipitation in the Atacama in March 2015. At least to a certain extent, their modeled and observed results match the strip-like patterns of InSAR coherence anomalies found for areas between Antofagasta and Calama in the period 2015 to 2016. Finally, [19] reported strip-like northwest–southeast-oriented patterns of low InSAR coherence in the southern Atacama Desert (north of Taltal). The anomalies were shown to be dependent on the prevailing wind direction, local precipitation, and to increased soil moisture or actual sediment transport. However, it remains ultimately unclear why the loss of

coherence appears as such narrow stripes. No detailed high resolution information on local extreme rainfall exists that would allow a direct comparison and validation. As pointed out by [19,33], strong rainfall events are characterized by a very high spatial variability, and CCD might simply capture this variability, at least to a certain extent.

Despite these tracked changes, which were accurately revealed by CCD and related to precipitation events with high magnitude overland flow and fluvial discharge, most of the analyzed area shows very high InSAR coherence over the whole time period. Even for temporal baselines of more than three years, most regions of the Atacama Desert are characterized by coherences values >0.8. Thus, areas of morphodynamic stability since 2015 can be identified, and these areas mostly lie, as assumed, in the hyperarid core of the Atacama Desert, where geologic and geomorphologic studies reveal very small erosion rates and generally low or even stagnant morphodynamic activity [23,60].

4.2. Short Temporal Baseline Time Series

The analysis of the temporally dense stack of Sentinel-1 acquisitions for the region of interest further revealed the high sensitivity of the InSAR coherence to the surface properties. The short temporal baselines led to very high InSAR coherences for most parts of the region, and generally very small signal variations were observed between 2016 and 2018, indicating stable and undisturbed surface properties, at least from a SAR perspective. However, differences between the geomorphic domains were observed, as these showed characteristic values of the mean coherence and intensity. These findings are summarized by the false color composite shown in Figure 10.

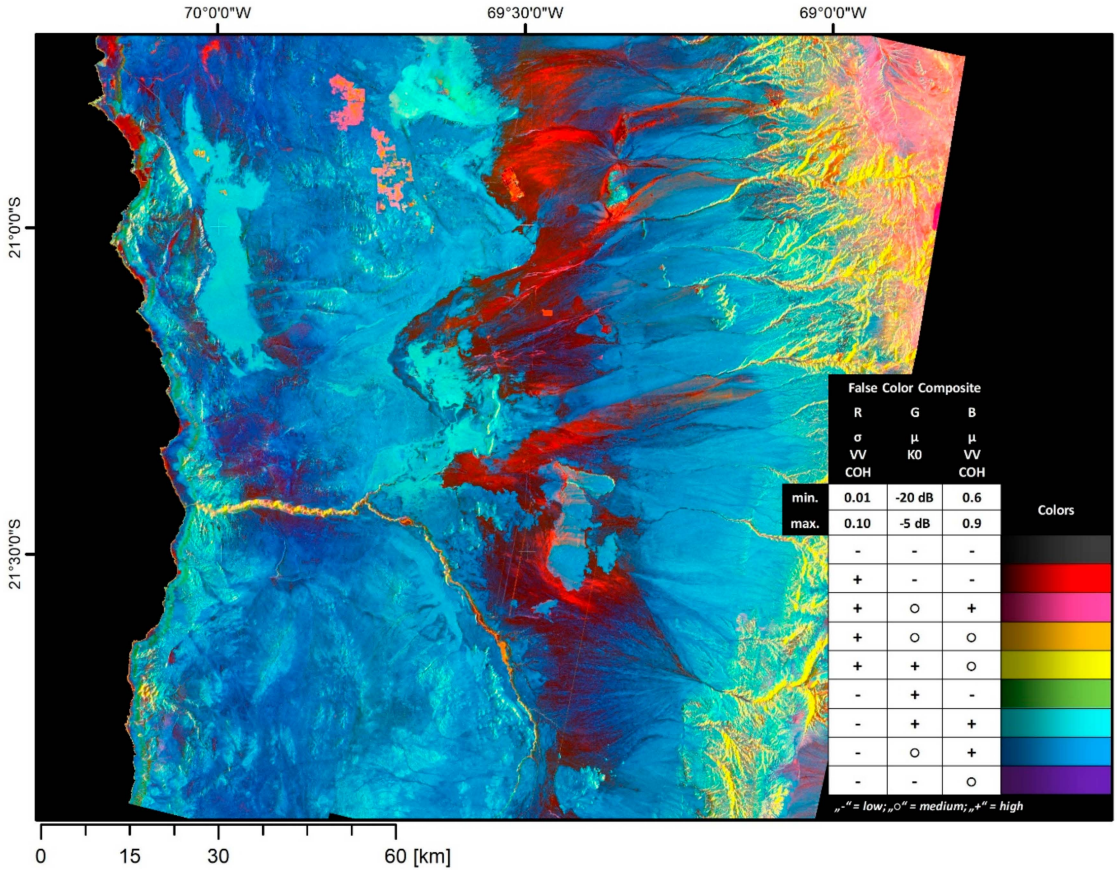

Figure 10. False color composite according to [8] for the simplified interpretation of short temporal baseline time series features of Sentinel-1: standard deviation of the VV InSAR coherence (σ COH VV) (red channel), mean total intensity (μ K0) (green channel), and mean VV InSAR coherence (μ COH VV) (blue channel). The features are linearly scaled to values of 0 to 255 for the given lower (min.) and upper thresholds (max.).

The composite was constructed according to [8] using σ COH VV (red), μ K0 (green), and μ COH VV (blue), but thresholds were modified to the characteristic values indicated above (Section 3.2.1). In the composite, yellowish colors indicate regions of high backscattering intensity but comparably low InSAR coherence and predominately designate regions affected by geometric distortions (i.e., layover and foreshortening). Bluish colors designate regions of very low temporal variability, but high to medium mean intensity and high mean InSAR coherence (e.g., paved or sealed surfaces, stable, consolidated, or nonvegetated surfaces). Dark reddish colors indicate surfaces that are characterized by high temporal variability and low to medium high mean intensity and low mean coherence. This signature is most frequently found over the alluvial plains of the Central Depression and over aeolian sandy deposits at the transition between the alluvial plains and the Precordillera. This observation is probably linked to the amount of fine-grained material; the associated higher potential soil-water content and smaller surface roughness [13] due to the slope position, as downslope locations are likely to have been more altered by recent morphodynamics [8]; and to the low scattering intensity, causing a low signal-to-noise ratio. Generally, patterns of more frequent signal variations were found along the Coastal Cordillera, whereas the central desert was characterized by very high signal stability, and variations of intensity and coherence were of very small magnitude.

Surface disturbances of high magnitude manifested in all of the investigated SAR features and were predominately caused by human activity. For example, regions containing mining activity were distinctly and clearly visible in the intensity and coherence imagery, due to exceptionally strong changes of the signal. Therefore, the SAR time series shows high potential for monitoring infrastructural development and (surficial) mining activity on a regular basis. Recently, human activity is causing the strongest and most extensive surface dynamics in the study area.

Similar, characteristic SAR signatures were found for sandy deposits and dunes. These manifest with the lowest observed InSAR coherences, beside water surfaces. This observation confirms the outcomes of preceding studies [13–15,17]. The active dune systems showed very low InSAR coherence for all temporal baselines, but high polarimetric entropy and very low intensity. Signal loss and phase decorrelation was observed over such areas, along with a high degree of depolarization, generating an exclusive SAR signature. On the one hand, the delineation of sandy aeolian deposits seems, therefore, highly feasible for the entire region, especially when intensity and InSAR coherence information is combined with topographic and multispectral information. On the other hand, this observation underlines that CCD is susceptible to causing ambiguities and false detections due to its high sensitivity to surface properties and the coherent formation of the signal, involving phase and intensity information. As pointed out by earlier studies [13,14], different types of surface cover cause a decorrelation of the SAR signal, independent of the temporal decorrelation. Such coverage can, in turn, be confused with temporal change-related decorrelation. It is, therefore, beneficial to gather knowledge on the temporal signal development by investigating temporally dense stacks (i.e., as they are offered by the Sentinel-1 mission). Ideally, such analysis should incorporate the InSAR coherences of different temporal baselines and periods. For instance, [19] shows that systematic investigations of coherence imagery of several different time periods and temporal baselines enables the estimation of temporal decay rates along with the classic CCD; however, this approach causes a high computational load.

The analyses further showed linear coherence anomalies at the transition from the Precordillera to the alluvial plain for the period December 2016 to March 2017. These anomalies again matched the reference channel network and are, therefore, interpreted to be caused by short-lasting fluvial activity. However, the event cloud may not be linked with documented large-scale precipitation events, and therefore it is assumed that the discharge was triggered by rainfall events further to the east in the Precordillera or by an increased ground water table in the Altiplano. The comparison to the optical datasets of Sentinel-2 showed that InSAR coherence is a well-suited feature to complement the detection of the on- and offset of discharge events (i.e., the variations of the coherence values were clear and distinct). As mentioned above, detection of such events via InSAR coherence requires a coherent "background".

The correlation assessment indicated that none of the SAR features were correlated with the morphometric features of the DEM to a high level of determination (R^2 <0.24). Thus, statistically the dependencies on the local topography are small. Nevertheless, it is observed that deeply incised gullies and steep slopes cause local inconsistencies and high variations of the InSAR coherence values over time that cannot be explained by natural phenomena. This limitation is related to the geometric distortions caused by the slant acquisition, which has already been pointed out by [14] (i.e., the application of CCD is more difficult, or even not possible, in mountainous and rugged terrain). Nevertheless, SAR features of intensity and coherence offer complementary data to the digital elevation model (and to multispectral data), and thus may be used as additional information to characterize and delineate landforms and zones that share similar surface characteristics or morphodynamic activity.

5. Conclusions

The analysis of Sentinel-1 time series (2015 to 2018) was conducted using long (365–1090 days) and short temporal baselines (12–24 days) in order to assess spatiotemporal variations on different time scales of InSAR coherence over the Atacama Desert (Chile). The Sentinel-1 orbital tube generated small and InSAR-suited perpendicular baselines that were in the range of several meters up to 140 m for all investigated datasets. Notably, perpendicular baselines for temporal baselines >300 days and >1000 days were in the order of 35 m, and the datasets were highly suited to generating extensive InSAR coherence mosaics covering the entire study area (approximately 450 × 1100 km). The mosaics were nearly seamless and very high phase stability in the C-Band of Sentinel-1 was observed for most parts of the region, indicating very stable surface conditions over time, especially over the hyperarid core of the Atacama Desert, which is characterized by very small erosion rates and low or even stagnant morphodynamic activity. Temporal baselines of several years only led to a very small decorrelation of the SAR signal and regions characterized by local signal decorrelation could be associated with certain types of surface cover (e.g., water or aeolian deposits) or with actual surface dynamics (e.g., due to anthropogenic disturbance, fluvial activity, or precipitation).

Strong precipitation events and fluvial activity in the periods 2015–2016 and 2017–2018 caused a significant signal decorrelation. In this context, the observed linear coherence anomalies perfectly match the reference channel network, and therefore indicated episodic or sporadic fluvial activity. In addition, an area-wide loss of InSAR coherence was observed along northwest–southeast-oriented strips. These anomalies were interpreted as the result of overland flow, or at least of a significant increase in soil moisture, due to the strong precipitation events in March and August of the 2015 El Niño phase and due to local events in the east and southeast of Antofagasta in June 2017. The spatial patterns of significant loss of coherence matched documented heavy precipitation events, with cumulative amounts of >20 mm. At the local level, short-term sporadic fluvial activity was observed in the coherence imagery in the period 2016–2018 using short temporal baselines (12 or 24 days). The differences in InSAR coherences before and after the discharge event were very distinct, and coherent change detection provides a promising method to capture fluvial events with high spatial and temporal detail. The investigations further confirmed the known signal decorrelation over aeolian deposits: sandy patches and dune systems showed very low InSAR coherences at all temporal baselines.

Considering the above findings, the Sentinel-1 data display great potential to contribute to recent geomorphological research. The analysis of dense Sentinel-1 time series allows capture and quantification of short-term sporadic and episodic processes of high magnitude that induce morphodynamic activity, especially fluvial activity. Thus, these SAR data seem to be suited for unravelling or monitoring recent geomorphic changes at local, regional, and supraregional scales; for upscaling local point data; and for characterizing geomorphic and geomorphodynamic domains in the Atacama Desert and other arid environments in future investigations.

Author Contributions: Conceptualization, T.U., D.H., and S.M.M.; data curation, T.U. and J.S.; formal analysis, T.U. and J.S.; funding acquisition, O.B.; investigation, T.U. and J.S.; methodology, T.U. and J.S.; project administration, R.B. and O.B.; software, T.U.; supervision, R.B. and O.B.; validation, T.U.; visualization, T.U.; writing—original draft, T.U. and J.S.; writing—review and editing, T.U., D.H., and S.M.M.

Funding: This research was funded by the German Research Foundation (Deutsche Forschungsgemeinschaft DFG), within the project "CRC 1211: Earth - Evolution at the Dry Limit", grant number 268236062™. TanDEM-X WorldDEM™ data was provided by the German Aerospace Center (DLR) via a science grant in 2017.

Acknowledgments: We thank Katharine Thomas for proofreading the manuscript. We thank the reviewers for their constructive and helpful comments.

Conflicts of Interest: The authors declare no conflict of interest. The funders had no role in the design of the study; in the collection, analyses, or interpretation of data; in the writing of the manuscript, or in the decision to publish the results.

References

1. European Space Agency (ESA). *Sentinel-1 ESA's Radar Observatory Mission for GMES Operational Services 2012*; SP-1322/1; ESA Communications: Oakville, ON, Canada, 2012; pp. 1–88.
2. European Space Agency (ESA). *Mission Requirements Document for the European Radar Observatory Sentinel-1*; ES-RS-ESA-SY-0007; European Space Agency: Paris, France, 2005; Volume 1, pp. 1–31.
3. Di Traglia, F.; Nolesini, T.; Ciampalini, A.; Solari, L.; Frodella, W.; Bellotti, F.; Fumagalli, A.; De Rosa, G.; Casagli, N. Tracking morphological changes and slope instability using spaceborne and ground-based SAR data. *Geomorphology* **2018**, *300*, 95–112. [CrossRef]
4. Ichoku, C.; Karnieli, A.; Arkin, Y.; Chorowicz, J.; Fleury, T.; Rudant, J.-P. Exploring the utility potential of SAR interferometric coherence images. *Int. J. Remote Sens.* **1998**, *19*, 1147–1160. [CrossRef]
5. Touzi, R.; Lopes, A.; Bruniquel, J.; Vachon, P.W. Coherence estimation for SAR imagery. *IEEE Trans. Geosci. Remote Sens.* **1999**, *37*, 135–149. [CrossRef]
6. Monti-Guarnieri, A.V.; Brovelli, M.A.; Manzoni, M.; d'Alessandro, M.M.; Molinari, M.E.; Oxoli, D. Coherent change detection for multipass SAR. *IEEE Trans. Geosci. Remote Sens.* **2018**, *56*, 6811–6822. [CrossRef]
7. Scheuchl, B.; Ullmann, T.; Koudogbo, F. Change Detection using high resolution TerraSAR-X data preliminary results. In Proceedings of the ISPRS Hannover Workshop, Hannover, Germany, 2–5 June 2009; pp. 1–4.
8. Ullmann, T.; Serfas, K.; Büdel, C.; Padashi, M.; Baumhauer, R. Data processing, feature extraction, and time-series analysis of Sentinel-1 synthetic aperture radar (SAR) imagery: Examples from damghan and bajestan playa (Iran). *Zeitschrift für Geomorphologie* **2019**, *62*, 9–39. [CrossRef]
9. Zebker, H.A.; Villasenor, J. Decorrelation in interferometric radar echoes. *IEEE Trans. Geosci. Remote Sens.* **1992**, *30*, 950–959. [CrossRef]
10. Plank, S. Rapid damage assessment by means of multi-temporal SAR—A comprehensive review and outlook to Sentinel-1. *Remote Sens.* **2014**, *6*, 4870–4906. [CrossRef]
11. Oxoli, D.; Boccardo, P.; Brovelli, M.A.; Molinari, M.E.; Monti Guarnieri, A. Coherent change detection for repeated-pass interferometric SAR images: An application to earthquake damage assessment on buildings. In *Proceedings of the ISPRS-International Archives of the Photogrammetry, Remote Sensing and Spatial Information Sciences*; Copernicus GmbH: Göttingen, Germany, 2018; Volume XLII-3-W4, pp. 383–388.
12. Washaya, P.; Balz, T.; Mohamadi, B. Coherence change-detection with Sentinel-1 for natural and anthropogenic disaster monitoring in urban areas. *Remote Sens.* **2018**, *10*, 1026. [CrossRef]
13. Wegmuller, U.; Strozzi, T.; Farr, T.; Werner, C.L. Arid land surface characterization with repeat-pass SAR interferometry. *IEEE Trans. Geosci. Remote Sens.* **2000**, *38*, 776–781. [CrossRef]
14. Liu, J.G.; Black, A.; Lee, H.; Hanaizumi, H.; Moore, J.M. Land surface change detection in a desert area in Algeria using multi-temporal ERS SAR coherence images. *Int. J. Remote Sens.* **2001**, *22*, 2463–2477. [CrossRef]
15. Catherine, B.; André, O. The use of SAR interferometric coherence images to study sandy desertification in southeast Niger: Preliminary results. In Proceedings of the Envisat Symposium 2007, Montreux, Switzerland, 23–27 April 2007; pp. 1–5.
16. Oyen, A.M.; Koenders, R.; Aria, S.E.H.; Lindenbergh, R.C.; Li, J.; Donselaar, M.E. Application of synthetic aperture radar methods for morphological analysis of the Salar De Uyuni distal fluvial system. In Proceedings of the 2012 IEEE International Geoscience and Remote Sensing Symposium, Munich, Germany, 22–27 July 2012; pp. 3875–3878.

17. Gaber, A.; Abdelkareem, M.; Abdelsadek, I.S.; Koch, M.; El-Baz, F. Using InSAR coherence for investigating the interplay of fluvial and aeolian features in arid lands: Implications for groundwater potential in Egypt. *Remote Sens.* **2018**, *10*, 832. [CrossRef]
18. Ullmann, T.; Büdel, C.; Baumhauer, R.; Padashi, M. Sentinel-1 SAR data revealing fluvial morphodynamics in damghan (Iran): Amplitude and coherence change detection. *Int. J. Earth Sci. Geophys.* **2016**, *2*, 1–14. [CrossRef]
19. Scott, C.P.; Lohman, R.B.; Jordan, T.E. InSAR constraints on soil moisture evolution after the March 2015 extreme precipitation event in Chile. *Sci. Rep.* **2017**, *7*, 4903. [CrossRef] [PubMed]
20. Houston, J.; Hartley, A.J. The central Andean west-slope rainshadow and its potential contribution to the origin of hyper-aridity in the Atacama Desert. *Int. J. Climatol.* **2003**, *23*, 1453–1464. [CrossRef]
21. Hartley, A.J.; Chong, G.; Houston, J.; Mather, A.E. 150 million years of climatic stability: Evidence from the Atacama Desert, northern Chile. *J. Geol. Soc.* **2005**, *162*, 421–424. [CrossRef]
22. Rundel, P.; Dillon, M.; Palma, B.; Mooney, H.; Gulmon, S.; Ehleringer, J. The phytogeography and ecology of the coastal Atacama and Peruvian deserts. *Aliso J. Syst. Evol. Bot.* **1991**, *13*, 1–49. [CrossRef]
23. Dunai, T.J.; López, G.A.G.; Juez-Larré, J. Oligocene–Miocene age of aridity in the Atacama Desert revealed by exposure dating of erosion-sensitive landforms. *Geology* **2005**, *33*, 321–324. [CrossRef]
24. Rech, J.A.; Currie, B.S.; Shullenberger, E.D.; Dunagan, S.P.; Jordan, T.E.; Blanco, N.; Tomlinson, A.J.; Rowe, H.D.; Houston, J. Evidence for the development of the Andean rain shadow from a Neogene isotopic record in the Atacama Desert, Chile. *Earth Planet. Sci. Lett.* **2010**, *292*, 371–382. [CrossRef]
25. de Porras, M.E.; Maldonado, A.; De Pol-Holz, R.; Latorre, C.; Betancourt, J.L. Late Quaternary environmental dynamics in the Atacama Desert reconstructed from rodent midden pollen records. *J. Quat. Sci.* **2017**, *32*, 665–684. [CrossRef]
26. Cereceda, P.; Larrain, H.; Osses, P.; Farías, M.; Egaña, I. The spatial and temporal variability of fog and its relation to fog oases in the Atacama Desert, Chile. *Atmos. Res.* **2008**, *87*, 312–323. [CrossRef]
27. del Río, C.G.; Rivera, D.S.; Siegmund, A.; Wolf, N.; Cereceda, P.; Larraín, H.; Lobos, F.; Garcia, J.L.; Osses, P.; Zanetta, N.; et al. ENSO influence on coastal fog-water yield in the Atacama Desert, Chile. *Aerosol Air Qual. Res.* **2018**, *18*, 127–144. [CrossRef]
28. Cereceda, P.; Osses, P.; Larrain, H.; Farías, M.; Lagos, M.; Pinto, R.; Schemenauer, R.S. Advective, orographic and radiation fog in the Tarapacá region, Chile. *Atmos. Res.* **2002**, *64*, 261–271. [CrossRef]
29. Clarke, J.D.A. Antiquity of aridity in the Chilean Atacama Desert. *Geomorphology* **2006**, *73*, 101–114. [CrossRef]
30. Matmon, A.; Quade, J.; Placzek, C.; Fink, D.; Arnold, M.; Aumaître, G.; Bourlès, D.; Keddadouche, K.; Copeland, A.; Neilson, J.W. Seismic origin of the Atacama Desert boulder fields. *Geomorphology* **2015**, *231*, 28–39. [CrossRef]
31. Owen, J.J.; Dietrich, W.E.; Nishiizumi, K.; Chong, G.; Amundson, R. Zebra stripes in the Atacama Desert: Fossil evidence of overland flow. *Geomorphology* **2013**, *182*, 157–172. [CrossRef]
32. Wilcox, A.C.; Escauriaza, C.; Agredano, R.; Mignot, E.; Zuazo, V.; Otárola, S.; Castro, L.; Gironás, J.; Cienfuegos, R.; Mao, L. An integrated analysis of the March 2015 Atacama floods. *Geophys. Res. Lett.* **2016**, *43*, 8035–8043. [CrossRef]
33. Jordan, T.E.; Herrera, C.; Godfrey, L.V.; Colucci, S.J.; Gamboa, C.; Urrutia, J.; González, G.; Paul, J.F. Isotopic characteristics and paleoclimate implications of the extreme precipitation event of March 2015 in northern Chile. *Andean Geol.* **2018**, *46*, 1–31. [CrossRef]
34. Rech, J.A.; Quade, J.; Hart, W.S. Isotopic evidence for the source of Ca and S in soil gypsum, anhydrite and calcite in the Atacama Desert, Chile. *Geochim. Cosmochim. Acta* **2003**, *67*, 575–586. [CrossRef]
35. Michalski, G.; Böhlke, J.K.; Thiemens, M. Long term atmospheric deposition as the source of nitrate and other salts in the Atacama Desert, Chile: New evidence from mass-independent oxygen isotopic compositions. *Geochim. Cosmochim. Acta* **2004**, *68*, 4023–4038. [CrossRef]
36. Ewing, S.A.; Sutter, B.; Owen, J.; Nishiizumi, K.; Sharp, W.; Cliff, S.S.; Perry, K.; Dietrich, W.; McKay, C.P.; Amundson, R. A threshold in soil formation at Earth's arid–hyperarid transition. *Geochim. Cosmochim. Acta* **2006**, *70*, 5293–5322. [CrossRef]

37. Wang, F.; Michalski, G.; Luo, H.; Caffee, M. Role of biological soil crusts in affecting soil evolution and salt geochemistry in hyper-arid Atacama Desert, Chile. *Geoderma* **2017**, *307*, 54–64. [CrossRef]
38. Abele, G. Salzkrusten, salzbedingte Solifluktion und Steinsalzkarst in der nordchilenisch-peruanischen Wüste. *Mainz. Geogr. Stud.* **1990**, *34*, 23–46.
39. Quade, J.; Reiners, P.; Placzek, C.; Matmon, A.; Pepper, M.; Ojha, L.; Murray, K. Seismicity and the strange rubbing boulders of the Atacama Desert, northern Chile. *Geology* **2012**, *40*, 851–854. [CrossRef]
40. May, S.M.; Hoffmeister, D.; Wolf, D.; Bubenzer, O. Zebra stripes in the Atacama Desert revisited—Granular fingering as a mechanism for zebra stripe formation? *Geomorphology* **2019**, *344*, 46–59. [CrossRef]
41. Cloude, S.R.; Pottier, E. A review of target decomposition theorems in radar polarimetry. *IEEE Trans. Geosci. Remote Sens.* **1996**, *34*, 498–518. [CrossRef]
42. Cloude, S. The dual polarisation entropy/alpha decomposition: A PALSAR case study. In Proceedings of the 3rd International Workshop on Science and Applications of SAR Polarimetry and Polarimetric Interferom, Frascati, Italy, 22–26 January 2007; pp. 1–6.
43. Schmitt, A.; Wendleder, A.; Hinz, S. The Kennaugh element framework for multi-scale, multi-polarized, multi-temporal and multi-frequency SAR image preparation. *ISPRS J. Photogramm. Remote Sens.* **2015**, *102*, 122–139. [CrossRef]
44. Zhang, Z.; Wang, C.; Zhang, H.; Tang, Y.; Liu, X. Analysis of permafrost region coherence variation in the Qinghai–Tibet plateau with a high-resolution TerraSAR-X image. *Remote Sens.* **2018**, *10*, 298. [CrossRef]
45. Mullissa, A.; Tolpekin, V.; Stein, A.; Perissin, D. Polarimetric differential SAR interferometry in an arid natural environment. *Int. J. Appl. Earth Obs. Geoinf.* **2017**, *59*, 9–18. [CrossRef]
46. Thomas, K. The tasselled cap—A graphic description of the spectral-temporal development of agricultural crops as seen by Landsat. In Proceedings of the Symposium on Machine Processing of Remotely Sensed Data, West Lafayette, IN, USA, 29 June–1 July 1976; pp. 1–11.
47. Kauth, C. The tasseled cap de-mystified. Transformations of MSS and TM data. *Photogramm. Eng. Remote Sens.* **1986**, *52*, 81–86.
48. Bozkurt, D.; Rondanelli, R.; Garreaud, R.; Arriagada, A. Impact of warmer eastern tropical pacific SST on the March 2015 Atacama floods. *Mon. Weather Rev.* **2016**, *144*, 4441–4460. [CrossRef]
49. European Space Agency (ESA). *Sentinel-2 User Handbook*; European Space Agency: Paris, France, 2015; pp. 1–64.
50. European Space Agency (ESA). *S2 MPC Sen2Cor Software Release Note*; S2-PDGS-MPC-L2A-SRN-V2.8.0; European Space Agency: Paris, France, 2019; Volume 2, pp. 1–77.
51. Deutsches Zentrum für Luft-und Raumfahrt (DLR). *TanDEM-X Ground Segment DEM Products Specification Document*; TD-GS-PS-0021; Deutsches Zentrum für Luft-und Raumfahrt: Cologne, Germany, 2016; pp. 1–46.
52. Gruber, A.; Wessel, B.; Huber, M.; Roth, A. Operational TanDEM-X DEM calibration and first validation results. *ISPRS J. Photogramm. Remote Sens.* **2012**, *73*, 39–49. [CrossRef]
53. Gonzalez, C.; Braeutigam, B.; Martone, M.; Rizzoli, P. Relative height error estimation method for TanDEM-X DEM products. In Proceedings of the EUSAR 2014; 10th European Conference on Synthetic Aperture Radar, Berlin, Germany, 3–5 June 2014; pp. 1–4.
54. Pipaud, I.; Loibl, D.; Lehmkuhl, F. Evaluation of TanDEM-X elevation data for geomorphological mapping and interpretation in high mountain environments—A case study from SE Tibet, China. *Geomorphology* **2015**, *246*, 232–254. [CrossRef]
55. Ullmann, T.; Büdel, C.; Baumhauer, R. Characterization of arctic surface morphology by means of intermediated TanDEM-X digital elevation model data. *Zeitschrift für Geomorphologie Supplementary Issues* **2017**, *61*, 3–25. [CrossRef]
56. Kramm, T.; Hoffmeister, D. A relief dependent evaluation of digital elevation models on different scales for northern Chile. *ISPRS Int. J. Geo Inf.* **2019**, *8*, 430. [CrossRef]
57. Gruber, S.; Peckham, S. Chapter 7 land-surface parameters and objects in hydrology. In *Developments in Soil Science*; Geomorphometry; Hengl, T., Reuter, H.I., Eds.; Elsevier: Amsterdam, The Netherlands, 2009; Volume 33, pp. 171–194.
58. Pelletier, J.D. *Quantitative Modeling of Earth Surface Processes*; Cambridge University Press: Cambridge, UK, 2008.

59. Segerstrom, K. Quaternary geology of Chile: Brief outline. *Geol. Soc. Am. Bull.* **1964**, *75*, 157. [CrossRef]
60. May, S.M.; Meine, L.; Hoffmeister, D.; Brill, D.; Medialdea, A.; Wennrich, V.; Gröbner, M.; Schulte, P.; Steininger, F.; Deprez, M.; et al. Origin and timing of past hillslope activity in the hyper-arid core of the Atacama Desert—The formation of fine sediment lobes along the chuculay fault system, Northern Chile. *Glob. Planet. Chang.* **2019**, *184*, 103057. [CrossRef]